HAL open science

Modeling of fluid-induced seismicity during injection and after shut-in

Qinglin Deng, Guido Blöcher, Mauro Cacace, Jean Schmittbuhl

▶ **To cite this version:**

Qinglin Deng, Guido Blöcher, Mauro Cacace, Jean Schmittbuhl. Modeling of fluid-induced seismicity during injection and after shut-in. Computers and Geotechnics, 2021, 140, pp.104489. 10.1016/j.compgeo.2021.104489 . hal-03873870

HAL Id: hal-03873870

https://hal.science/hal-03873870v1

Submitted on 16 Oct 2023

HAL is a multi-disciplinary open access archive for the deposit and dissemination of scientific research documents, whether they are published or not. The documents may come from teaching and research institutions in France or abroad, or from public or private research centers.

L'archive ouverte pluridisciplinaire **HAL**, est destinée au dépôt et à la diffusion de documents scientifiques de niveau recherche, publiés ou non, émanant des établissements d'enseignement et de recherche français ou étrangers, des laboratoires publics ou privés.

Distributed under a Creative Commons Attribution - NonCommercial 4.0 International License

Version of Record: https://www.sciencedirect.com/science/article/pii/S0266352X21004730
Manuscript_9ed733b7148f9c013553c78df39c6501

Modeling of fluid-induced seismicity during injection and after shut-in

Qinglin Deng[1,*], Guido Blöcher[2], Mauro Cacace[2], Jean Schmittbuhl[1]

Abstract

We develop a fully coupled hydro-mechanical model to simulate fault slip due to fluid injection. We consider the interaction between a hydraulic fracture and pre-existing faults as well as the fluid exchange between the fracture/fault and the porous matrix. In order to consider a pressure diffusion mechanism, we set a relatively high permeability around the stimulated path. Our parametric study shows that a couple of factors affect the fault activation and its slip behavior such as fault properties, friction properties and injection scenario. We observe that pore pressure diffusion induces poroelastic stress change, which are able to produce shut-in events with a time and space lag. This mechanism also affects the slip behavior during injection in particular when the surrounding permeability is high (e.g., up to 1e-13 m^2/s), and provides a new insight into understanding the occurrence of stronger seismic events after shut-in compared to the injection phase. In addition, we show that small perturbations may trigger large seismic fault slip which highlights the key role of the initial fault stress state. The results have profound implications for deep fluid injection related engineering as well as for soft cyclic injection strategies aiming to mitigate the risk of large earthquakes.

Keywords: hydraulic stimulation, hydro-mechanical coupling, fault reactivation, induced seismicity, pore pressure diffusion, shut-in effect

*Corresponding author
Email address: dengq@unistra.fr (Qinglin Deng)
[1]EOST/ITES, Université de Strasbourg/CNRS, France
[2]GFZ German Research Centre for Geosciences, Potsdam, Germany

© 2021 published by Elsevier. This manuscript is made available under the CC BY NC user license
https://creativecommons.org/licenses/by-nc/4.0/

1. Introduction

Hydraulic stimulation has been applied in many underground engineering projects, such as coalbed methane mining (McDaniel et al., 1990; Colmenares and Zoback, 2007), oil/gas recovery (Law et al., 1993; Barati and Liang, 2014), shale gas production (Johri and Zoback, 2013; Lei et al., 2017), waste water disposal (Keranen et al., 2014; Brudzinski and Kozłowska, 2019) as well as deep geothermal energy extraction (Fehler, 1989; Murphy et al., 1999; Evans et al., 2005; Gaucher et al., 2015; Schill et al., 2017). It has been proven to be effective to improve fracture connectivity, increase reservoir transmissivity and enhance fluid circulation. However, due to high pressure fluid injection, such operation is often accompanied by seismic activities. Sometimes they can be felt by people on the ground and destroy ground facilities, therefore cause strong social disputes (Majer et al., 2007; Häring et al., 2008; Langenbruch et al., 2018; Lee et al., 2019; Lei et al., 2019). Furthermore, those man-made earthquakes not only occur during the injection phase, but also after the operation termination, termed as 'post injection induced seismicity', which can be observed both from the laboratory and the field (Stanchits et al., 2011; Hsieh and Bredehoeft, 1981; Evans et al., 2005; Albaric et al., 2014). The post injection induced seismicity sometimes exhibits discontinuities both in time and space. For instance, the hydraulic stimulation performed in June 2013 in the Rittershoffen geothermal site induced seismicity during injection but a second swarm of events occurred over 100 meters away from the first earthquake sequence 4 days after shut-in (Lengliné et al., 2017). Moreover, these additional seismic events may

have large magnitude, some of them are even stronger than the seismicity during the injection (Häring et al., 2008; Baisch et al., 2010; Albaric et al., 2014; McClure, 2015; Baujard et al., 2017). Those observations increase the uncertainty and complexity of the hydraulic operation response, and pose a challenge for earthquake risk prediction and control.

Over the past few decades, a large number of researchers have been devoted to study fluid-induced seismicity mechanisms and its hazard control, across scales ranging from $\sim$ cm to $\sim$ km. Those studies are based on either a statistical (Shapiro et al., 1999; Parotidis et al., 2004; Barth et al., 2013) or physical description of the induced dynamics. Physics based investigation comprises laboratory experiments (Stanchits et al., 2011; Passelègue et al., 2018; Ji et al., 2019; Wang et al., 2020), field tests (Cornet and Jianmin, 1995; Blöcher et al., 2018; De Barros et al., 2019), as well as numerical modeling (Baisch et al., 2010; Yoon et al., 2017; Maurer et al., 2020). The main triggering mechanisms for injection-induced seismicity, can be attributed to pore pressure diffusion (Shapiro et al., 1999; Brown and Ge, 2018), poroelastic stress response (McClure and Horne, 2011; Chang and Segall, 2016; Jacquey et al., 2018), aseismic slip (Guglielmi et al., 2015; Lengliné et al., 2017), as well as earthquake interactions (Yeo et al., 2020). Yet other mechanisms are also reported to be responsible for post-injection induced seismicity, such as the superposed stress variations (De Simone et al., 2017) and fracture normal closure (Ucar et al., 2017).

Although those studies have formed the basic framework of fluid injection induced seismicity, none of them can deal with all cases due to the complexity of the underground structure and the coupling process. Some questions, e.g.,

the role of related control parameters, have been partially answered and still need to be further investigated. Thus, it is of primary importance to explore the multi-physical processes undergoing in deep reservoirs from the injection stage to the post injection stage, in order to minimize the risk of earthquakes and achieve successful hydraulic stimulation.

The goal of a hydraulic stimulation is to stimulate permeability enhancement in the reservoir. As such it requires a good conceptual model for the stimulation. Currently, there are four main stimulation mechanisms are considered: (i) pure opening (tensile) mechanism, aiming to create new fractures (i.e., hydro-fracturing) (Zoback et al., 1977; Ren et al., 2015); (ii) pure shear mechanism, which assumes that the stimulation mainly acts on the shear slip of the pre-existing fractures (Xie and Min, 2016; Ye and Ghassemi, 2018); (iii) primary fracturing with shear stimulation leakoff, under which new fractures are continuously created and propagated from the wellbore with fluid leaks off into natural fractures (Pearson, 1981; Wang et al., 2018); (iv) the mixed mechanism, i.e., flow pathways are connected with both newly created and pre-existing fractures (Norbeck et al., 2016; Lei et al., 2021). Since different communities tend to rely on a different stimulation concept. For example, the opening mode is commonly the preferred stimulation in oil/gas industry, while hydro-shearing is widely used in the context of Enhanced Geothermal System (EGS). Numerous field observations are also supportive of the benefit from the mixed stimulation (Albaric et al., 2014; Norbeck et al., 2018; Krietsch et al., 2020). Moreover, a recent study also suggests an important role of the stress transfer from hydraulic fracture opening in induced seismicity distribution (Kettlety et al., 2020).

In the context of the mixed stimulation strategy, there are two processes that could trigger seismicity, that is, the brittle failure of intact rocks by hydro-fracturing (HF) and the activation of pre-existing fractures. It has been evidenced that HF-induced seismicity in terms of magnitude is negligible compared to the fault shearing induced seismicity (Zoback, 2010; Lei et al., 2021). Hence, many studies only focus on the shear slip of natural fractures in fluid injection-induced seismicity (McClure and Horne, 2011; Rutqvist et al., 2013; Yoon et al., 2017).

In this study, we aim at investigating fault slip behavior during active fluid injection and after shut-in. We develop a fully hydro-mechanical coupling model for a fractured porous rock while considering the interaction between existing faults and the hydraulic fractures. In doing so, we consider only a single path for the stimulated fracture thereby being able to better control the model behavior. In section 2, basic governing equations are described. Section 3 introduces the model setup for the simulations, which is followed by results with parametric studies on the permeability of fracture damage zone (FDZ), the fault friction coefficient, fault orientation, as well as different injection scenarios. Further discussion and main conclusions are given in section 4 and section 5, respectively. A validation of hydraulic fracture propagation is also presented in the end.

2. A coupled hydro-mechanical cohesive zone model

Generally, when involving hydraulic fracturing, there are four physical processes to be considered, i.e., porous rock mass deformation, pore fluid flow, fracture fluid flow and fracture propagation (Carrier and Granet, 2012).

For problems which involve interactions with pre-existing faults, the fault slip should also be defined (Chen et al., 2017; Li et al., 2017).

2.1 Porous media deformation

Under isothermal conditions, rock mass is considered as an isotropic, poroelastic material. Assuming small strains, the poro-elastic constitutive relation is expressed as (Coussy, 2004):

$$\sigma_{ij} - \sigma_{ij,0} = 2G\varepsilon_{ij} + \left(K - \frac{2}{3}G\right)\epsilon\delta_{ij} - b(p - p_0)\delta_{ij} \tag{1}$$

where σ_{ij} and ε_{ij} are the total stress and strain; ϵ the volumetric strain; p the pore pressure; G and K are the dry elastic shear and bulk moduli, and b the Biot's coefficient. The subscript '0' represents the initial state of each variable.

Eq. (1) in terms of effective stress can be simplified to:

$$\sigma_{ij}^{'} - \sigma_{ij}^{'0} = 2G\varepsilon_{ij} + \left(K - \frac{2}{3}G\right)\epsilon\delta_{ij} \tag{2}$$

Following Biot's theory (Biot, 1941), the effective stresses tensor defined for fully saturated media as:

$$\sigma_{ij}^{'} = \sigma_{ij} - bp\delta_{ij} \tag{3}$$

2.2 Pore fluid flow

It is assumed that fluid flows through an interconnected pore network following Darcy's law:

$$q = -\frac{k}{\eta}\nabla p \tag{4}$$

where q is the Darcy's velocity, η is the pore fluid dynamic viscosity, and k is the permeability.

The continuity flow equation for the fluid within the pores is given by:

$$\frac{1}{M_b}\frac{\partial p}{\partial t} + b\frac{\partial \epsilon}{\partial t} + \nabla \cdot q = 0 \tag{5}$$

where M_b is Biot's modulus defined by:

$$\frac{1}{M_b} = \frac{\phi_0}{K_f} + \frac{b - \phi_0}{K_s} \tag{6}$$

where K_f, K_s donates the pore fluid bulk modulus and the porous medium solid grain bulk modulus, and ϕ_0 is the initial porosity.

Combining with Eq. (4) and Eq. (5), the pore fluid diffusion equation is obtained as follows:

$$\frac{1}{M_b}\frac{\partial p}{\partial t} + b\frac{\partial \epsilon}{\partial t} = \frac{k}{\eta}\nabla^2 p \tag{7}$$

2.3 Fluid flow inside the fracture

Assuming Newtonian and incompressible fluid, the flow inside a fracture can be split into a tangential flow within the fracture and a normal flow across the fracture walls, as shown in Fig. 1.

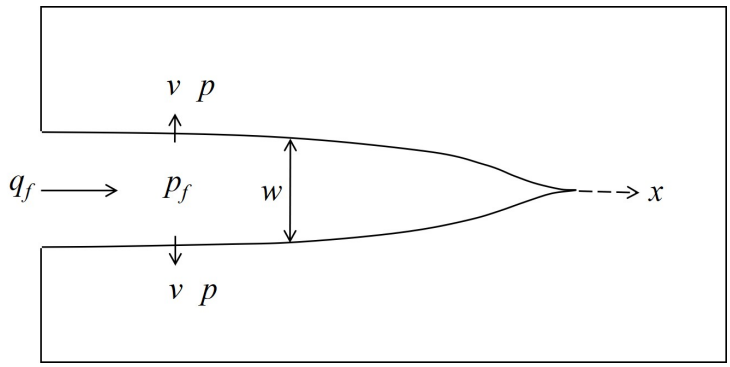

Fig. 1. Fluid flow model of the fracture

The tangential flow is governed by Reynold's lubrication theory defined by the continuity equation (Detournay, 2004):

$$\frac{\partial w}{\partial t} + \frac{\partial q_f}{\partial x} + v = 0 \tag{8}$$

where w is the fracture aperture, q_f is the longitudinal fluid flow rate, and v denotes normal flow rate leaking into the porous medium through the fracture surfaces. The latter parameter can be calculated from the difference between the fluid pressure inside the fracture p_f and the pore fluid pressure:

$$v = c\,(p_f - p) \tag{9}$$

where c is the leak-off coefficient. Eq. (9) imposes a pressure continuity between the fracture and the rock and defines a pressure-flow relationship between the cohesive element's middle nodes and its adjacent surface nodes. In homogeneous porous reservoirs, leakoff only occurs normal from the fracture into the pore system. This kind of leakoff can be described by Carter's leakoff model considering a filter-cake zone, an invaded zone, and a reservoir compaction zone (Howard and Fast, 1957; Liu et al., 2016). In such a model the leakoff coefficient as shown in Eq. (9) is pressure independent. In the case of additional natural fractures, the physics of leakoff will alter due to pressure dependent flow behavior of the fracture. In that case the leakoff coefficient becomes pressure dependent (Liu et al., 2016). In our study we only consider the first scenario, the pressure diffusion from a fracture into a porous matrix and henceforth only consider a pressure independent leakoff coefficient (Eq. 9). In addition, as leak-off coefficient and permeability increase, the fracture length decreases (Yao, 2012). When the permeability and the leak-off coefficient are sufficient small, the effect on the fracture length

will be negligible. In this work, considering the range of permeability ($\leq$ 1e-13 m^2), we set the leak-off coefficient 1e-11 m^3/kPa·s, e.g., Yao (2012).

Assuming the fracture walls are parallel and smooth, the longitudinal fluid flow rate q_f is related to the pressure gradient inside the fracture as (the Poiseuille law):

$$q_f = -\frac{w^3}{12\eta}\frac{\partial p_f}{\partial x} \tag{10}$$

where q_f is the flow flux inside the fracture.

Substituting Eq. (9) and Eq. (10) into Eq. (8) yields the governing equation of the fluid flow inside the frature:

$$\frac{\partial w}{\partial t} + v = \frac{\partial}{\partial x}\left(\frac{w^3}{12\eta}\frac{\partial p_f}{\partial x}\right) \tag{11}$$

2.4 Fracture initiation and propagation

For hydraulic fracturing, coupled stress-pressure cohesive elements with displacement and pore pressure degrees of freedom (DOFs) are simultaneously used. They are embedded in solid continuum elements (also with pressure DOF) to define a predefined crack path, such that the fracture growth is constrained to this path. Cohesive elements have been widely used to study fracture problems in rock-like materials (Zhuang et al., 2014; Saadat and Taheri, 2019). During the fracture propagation, a small fracture process zone (FPZ) is formed to capture stress concentration around the crack tip. In this study, we assume the damage initiation and evolution follow a linear traction-separation law (Fig. 2). The relation between the traction T and the separation δ is given by (Yao, 2012):

$$T = (1 - D)K_0\delta \tag{12}$$

where $D(0 \leq D \leq 1)$ is the damage variable and K_0 is a penalty stiffness, introduced to avoid total compliance of the whole model before initiation (Turon et al., 2007).

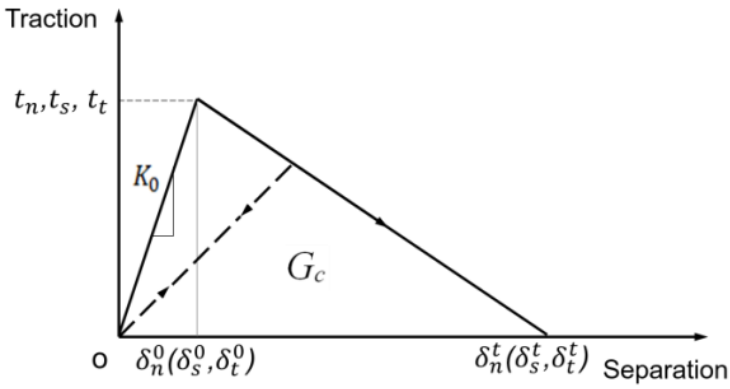

Fig. 2. Linear elastic traction-separation cohesive model

The total separation (i.e., fracture propagation) is depend on the fracture energy G_c and the damage initiation is determined by the maximum nominal stress criterion:

$$max\left\{\frac{< t_n >}{t_n^0}, \frac{t_s}{t_s^0}, \frac{t_t}{t_t^0}\right\} = 1 \tag{13}$$

where t_n^0, t_s^0, t_t^0 is the peak value of the nominal stress when the deformation is either purely normal to the interface or purely in the first or the second shear direction, respectively. The Macaulay bracket symbol "<>" signifies that a pure compressive stress does not initiate damage.

2.5 Fault slip

The Coulomb friction law is used to model the shear slip behavior of fault. Assuming the cohesion strength of the fault surface is negligible, i.e., for a cohesion-less fault, the shear strength τ_c is changing with the normal stress

σ_n as follows:

$$\tau_c = \mu \cdot (\sigma_n - p) \tag{14}$$

where μ is the coefficient of friction. Typically, μ varies between 0.6 and 1 for intact rock, 0.3 and 0.6 or even lower for pre-existing faults (Zoback, 2010; Ellsworth, 2013; Gaucher et al., 2015). In this work, $\mu = 0.2$, 0.4 and 0.6 are selected for parametric study.

As long as the shear stress exceeds the fault shear strength, the fault becomes unstable and slips along the fault plane. There are several causative processes responsible for the shear slip. For example, an increase in the shear stress, a reduction in the effective normal stress, or a decrease in the friction coefficient. The induced shear slip is often accompanied by the release of stored strain energy, hence induces seismicity.

3. Model setup

We consider hydraulic stimulation based on the assumption of mixed mechanism (i.e., both fracture opening and shearing). As shown in Fig. 3(a), we define two pre-existing faults F1 and F2 (blue solid line) in a 2D model. Those two faults are connected with potential hydraulic fracturing paths (blue dashed line), which are assumed to be parallel to the maximum principle stress σ_1 (Zoback, 2010). Each individual segment has a length of 10 m and both faults are oriented at a degree of α, where α is the angle between the maximum principal stress σ_1 and the fault plane. All boundaries are fixed with zero displacement and initial pore pressure of the model. The injection point is located at the bottom of the model (red dot) and fluid is injected at a flow rate Q. To investigate the after shut-in effect, we intentionally set

the stop position between F1 and F2 (black dot). It will not exceed the half length of the segment (5 m) from F1 in all the simulations. To precisely describe the pore pressure diffusion, we set a relatively permeable zone near the faults and hydraulic paths (black dashed lines) for which we assumed a constant width (1 m). It is modeled by an increased permeability (considered as an effective value averaging local micro-structural heterogeneities) than the intact rock matrix, similar to the fault damage zone (FDZ) (Evans et al., 1997; Nara et al., 2011; Mitchell and Faulkner, 2012; Hearn et al., 2018), where the fracture density is high. In addition, we also consider an exchange of fluid mass from the fractures to the permeable zone, in order to explore the impact of its permeability (linked with pressure diffusion) on the fault slip.

At the intersection of hydraulic fracturing path and fault, we assume that the fluid is directly diverted to the fault. This assumption is supported by previous studies which indicated that for a ratio of the initial maximum to the minimum stress larger than 1, and for a friction coefficient smaller than 0.65 and fracture orientation lower than 45°, a hydraulic fracture will be diverted into the pre-existing fault (Gu et al., 2012).

In addition, the porous medium is assumed to be fully saturated. The simulations are performed in Abaqus package. All parameters used are listed in Tab. 1.

4. Results and analysis

Fig. 4 shows the fluid pressure distribution at different time, and Fig. 5 presents the fluid pressure evolution at the injection point and the center of

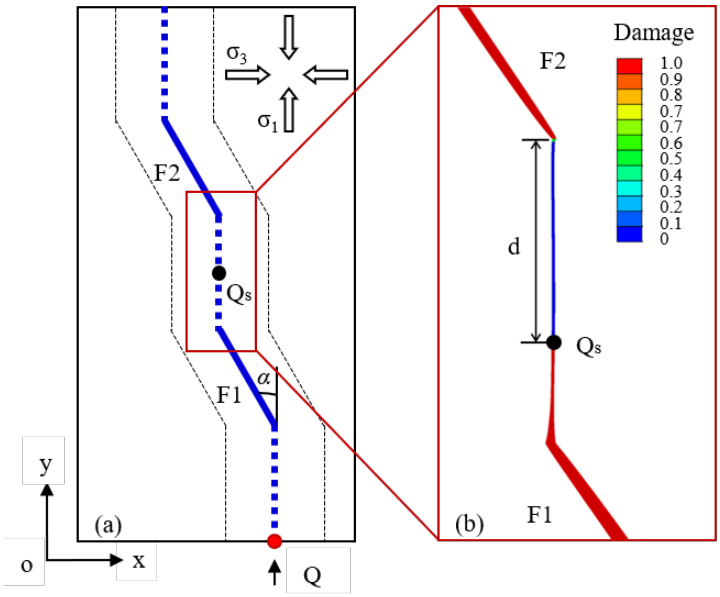

Fig. 3. (a) Geometry of the conceptual model. The red dot represents the injection point. The blue dashed line and blue solid line indicate hydraulic fracturing paths and pre-existing faults, respectively. Each segment is 10 meters long. The two parallel black dashed lines denote permeable fault damage zone. (b) Schematic diagram of induced fault slip during and after injection. The point Q_s represents the stop injection position. d is the quiescence space between Q_s and the fault F2. The red and blue color denotes the damage variable $D = 1$ and $D = 0$, which indicates fully damage and zero damage respectively.

Table 1. Initial input material properties

Property	**Symbol**	**Value**	**Unit**	**Notes**
Young's modulus	E	37.5	GPa	(Meyer et al., 2017)
Poisson ratio	v	0.25	-	(Meyer et al., 2017)
Porosity	ϕ	0.01	-	-
Rock permeability	k	1.0e-16	m^2	-
Permeability near fault	k_f	1.0e-15	m^2	-
Fracture Energy	G_c	80	Pa·m	-
Tensile strength	T_c	2	MPa	-
Penalty stiffness	K_0	800	GPa/m	(Turon et al., 2007)
Biot's coefficient	b	1.0	-	-
Friction coefficient	μ_1, μ_2	0.2	-	-
Fault orientation	α_1, α_2	30	°	-
Initial aperture	w	0.4	mm	(Meyer et al., 2017)
Fluid viscosity	η	0.001	Pa·s	water
Leak-off coefficient	c	1.0e-11	m^3/kPa·s	(Yao, 2012)
Saturated degree	s	100	%	-
Initial maximum stress	σ_1	36	MPa	(Meyer et al., 2017)
Initial minimum stress	σ_3	29	MPa	(Meyer et al., 2017)
Initial pore pressure	p_0	23.7	MPa	(Meyer et al., 2017)
Injection rate	Q	0.001	$m^3 \cdot s^{-1}$	-
Injection time	t_i	160	s	-
Shut-in time	t_s	600	s	-

F1, F2. The fault F1 is activated at 38.1 s while F2 is triggered at 520.1 s (i.e., 360.1 s after shut-in). This can be identified by the damage variable (Fig. 3b).

At the beginning, due to high-pressure fluid stimulation, the injection pressure rises to approximately 67 MPa from an initial value 23.7 MPa in a very short time ($\approx$ 2.7 s). Due to this drastic pressure change, the induced tensile stress is sufficient to overcome the rock tensile strength. As the hydraulic fracture propagates, the fluid pressure tends to drop to a stable level. Meanwhile, the fluid pressure at the center of F1 and F2 increases, since the high-pressure fluid inside the hydraulic fracture leaks into the surrounding porous rock mass and then diffuses all around. At 38.1 s (point A in Fig. 5), the injected water diverts to F1, which lowers the injected pressure and forces the fluid pressure of F1 to increase. This is accompanied by a shear slip along F1 as its shear strength is overcome by the high pressure (see Fig. 8a). Meanwhile, the pressure in the center of F2 witnesses a slight jump due to poro-elastic effect. Immediately afterwards, the pressure within F1 also decreases due to the generation of a new hydraulic fracture from the end of F1. This pressure drop in regions near fracture intersections is a common feature which has been already observed by other authors, e.g., Piris et al. (2018). From this time onward, the fluid pressures at injection point and F1 almost remain a same level with a tiny difference owing to the fluid flowing into the matrix. After 160 s of injection (point B in Fig. 5), the pumping stops and the fluid pressure starts to decrease. Pore pressure diffusion away from the pressurized hydraulic fracture can indeed be clearly observed (Fig. 6a). After approximately 360.1 s of termination of the injec-

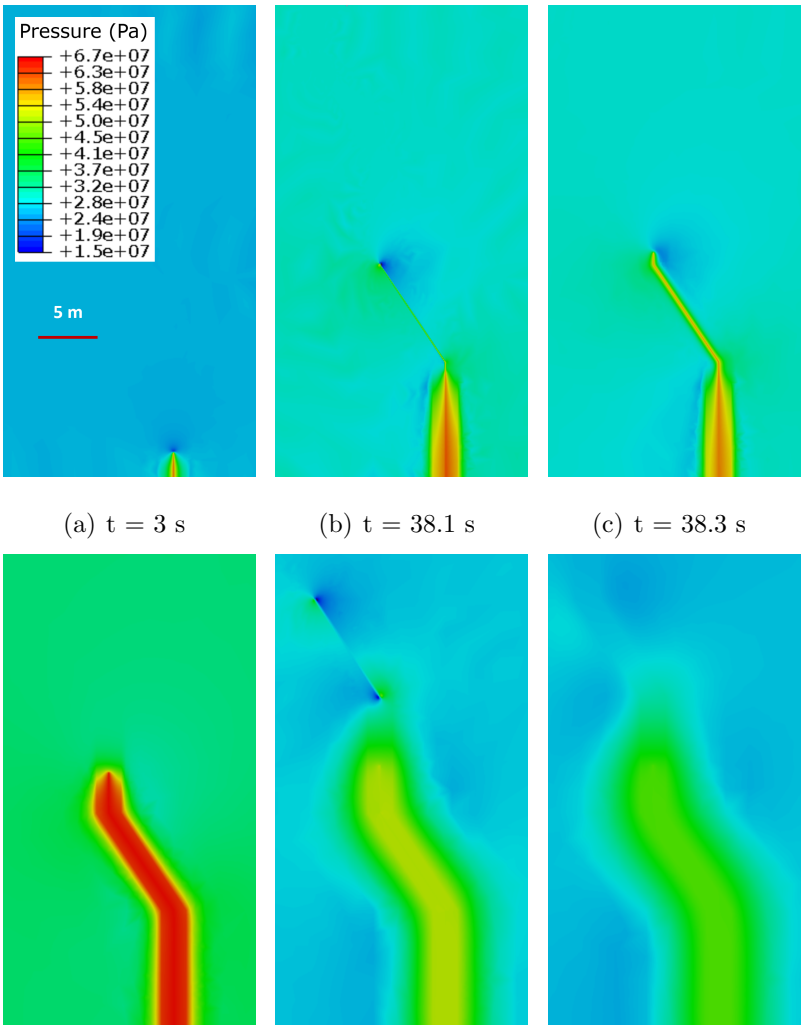

(a) t = 3 s (b) t = 38.1 s (c) t = 38.3 s

(d) t = 160 s (e) t = 520.1 s (f) t = 760 s

Fig. 4. Pore pressure distribution during injection and after termination. (a) onset of the injection; (b) F1 activation; (c) the second hydraulic fracture initiation; (d) stop injection; (e) F2 activation; (f) pore pressure diffusion in the porous rock matrix

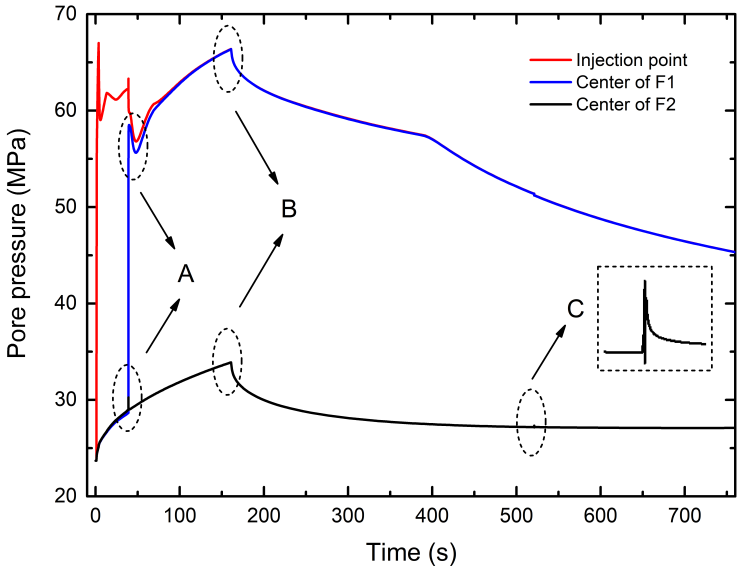

Fig. 5. Pore pressure evolution at the injection point and the center of fault F1 and F2

tion, the pressure perturbation and the corresponding stress change promote instability along the fault. As the fault slips, a compressional zone and a dilation zone emerge around the fault tip (Fig. 6). High pressure and stress in the compressional zone and low pressure and stress in the dilation zone are observed, respectively. This leads to only a minor increase in pressure at the F2 center (point C in Fig. 5), but to a rather significant increase at Node 2 within the compressional zone (point C in Fig. 7). See also Fig. 6 for their relative locations. This poro-elastic stressing mechanism is similar to the one described by injection into a single fracture embedded in a poro-elastic medium (Lei et al., 2021), and the combined induced fault slip mechanism (i.e., interaction between delayed pressure diffusion and poro-elasticity) during shut-in is in agreement with the results from previous investigation, e.g., Chang et al. (2018).

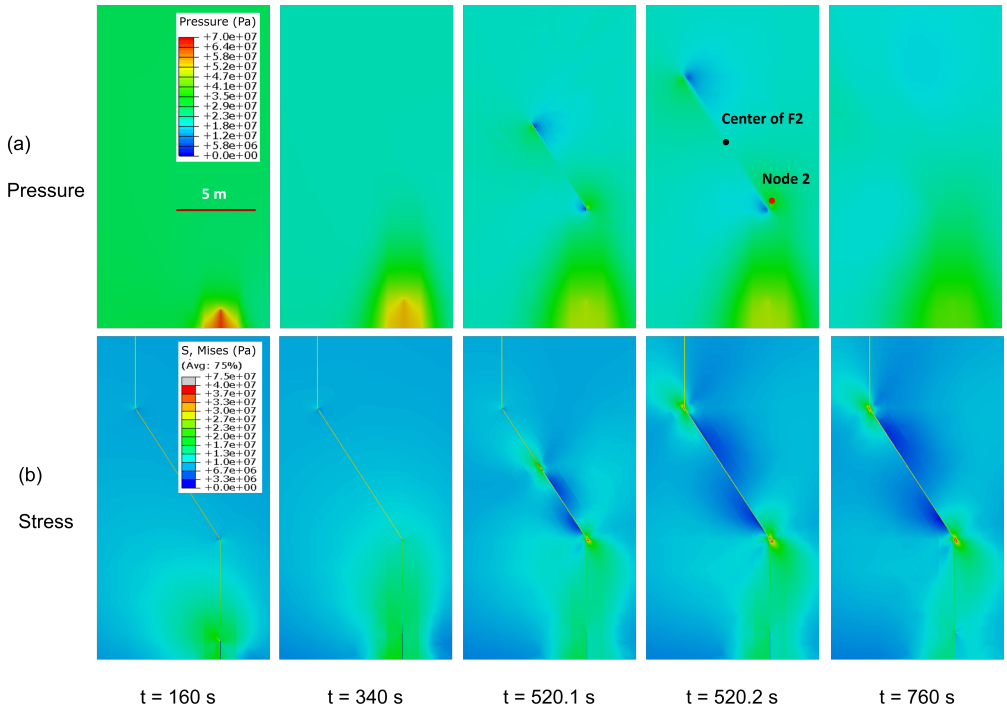

Fig. 6. Evolution of (a) pressure and (b) stress of F2 during shut-in stage

In fact, the sudden elevated fluid pressure, either owing to direct injection in F1 or pressure diffusion/poro-elasticity for F2, counteracting the normal stress and inducing dynamic slip of the fault, which correlates to potential micro-seismic events. The evolution of slip and slip rate of F1 and F2 over time is presented in Fig. 8. The characterization of displacement jump and slip rate rise is similar to an unloading experiment of a sawcut fracture (Ji et al., 2019). It can also be seen that in most of time the slip rates of F1 and F2 are close to zero, indicating an aseismic behavior. The seismic and aseismic slip is distinguished with a slip velocity threshold 5 mm/s (McClure and Horne, 2011; Cappa et al., 2018). In the following, the seismic slip and

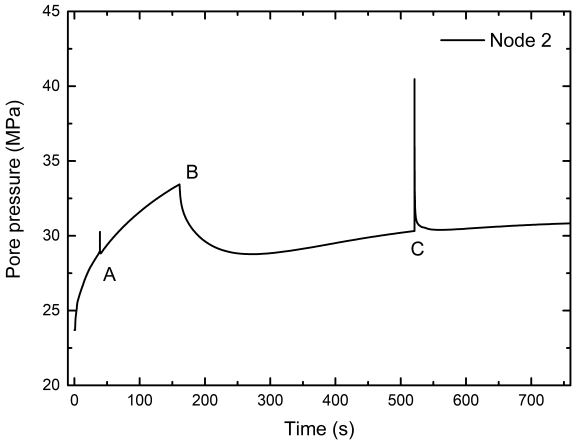

Fig. 7. Pore pressure evolution of Node 2 in the compressional zone

the associated average slip rate are calculated for each case.

4.1 Permeability of the fault damage zone

Pore pressure diffusion in a fractured porous medium is of central importance in fluid injection in faulted reservoirs (Chang and Segall, 2016; Shapiro et al., 1999). The core controlling parameter is the hydraulic diffusivity, which is related to the permeability (Deng et al., 2021; Shapiro et al., 1999). In order to investigate the impact of the hydraulic pressure diffusion on the fault slip, we carry out a systematic analysis on the role of the fault damage zone (FDZ) permeability by varying its value within three steps, that is, k_{f1} = 1e-15 m^2, k_{f2} = 5e-15 m^2 and k_{f3} = 1e-14 m^2. We perform several simulations at each permeability by altering the injection duration, in order to capture the activation of F2 after shut-in. The corresponding results are summarized in Tab. 2.

Table 2. Summary of key parameters and results with different permeability within the damage zone

Case*	**Injection time (s)**	**Permeability of FDZ (m^2)**	**Slip onset of F1 (s)**	**Slip onset of F2 (s)****
A1	150	1.0e-15	38.12	-
A2	160	1.0e-15	38.12	360.1
A3	165	1.0e-15	38.12	188.1
A4	170	1.0e-15	38.12	74.5
A5	120	5.0e-15	42.01	-
A6	130	5.0e-15	42.01	199.4
A7	140	5.0e-15	42.01	86.0
A8	160	5.0e-15	42.01	34.7
A9	100	1.0e-14	35.83/47.81	-
A10	110	1.0e-14	35.83/47.81	141.4
A11	130	1.0e-14	35.83/47.81	25.2
A12	160	1.0e-14	35.83/47.81	150.8 (in)

* all cases have fault orientation $\alpha = 30°$, friction coefficient $\mu_1 = \mu_2 = 0.2$, injection rate Q = 0.001 m^3/s;

** the slip time of F2 specifies the time after termination; F2 slip during injection is marked as '(in)'. All the same below.

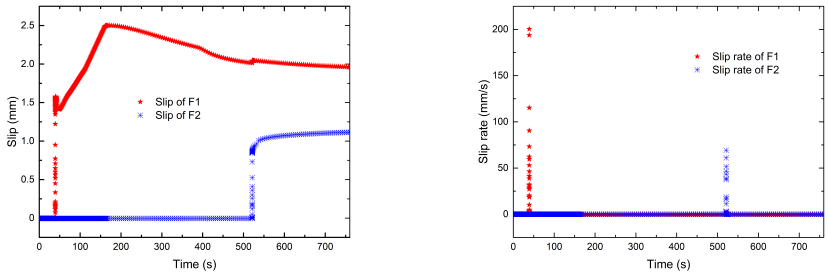

(a) (b)

Fig. 8. Evolution of (a) total slip and (b) slip rate of F1 and F2 over time

It is worth noting that the permeability of FDZ is higher than the matrix permeability (1e-16 m^2) hence allows faster pore pressure diffusion in the damage zone. The time at which the hydraulic fracture intersects F1 scales with the permeability, since higher permeability values promote faster diffusion and therefore a slower fracture propagation (Carrier and Granet, 2012). Meanwhile, due to fluid leak-off from the hydraulic fracture into the matrix, the pressure front propagates faster than the hydraulic fracturing front (Fig. 9). Here, the pressure front is defined as the pressure contour above the initial pore pressure. We noticed that when the matrix permeability is relatively low (case A2 and A8), the difference in the timing between the two propagating fronts is small (Fig. 9a and Fig. 9b). When the permeability is high (case A12), the pressure front significantly exceeds the fracturing front (Fig. 9c). If the leak-off is ignored (e.g., the KGD problem described in the Appendix A), the pressure front and the fracturing front coincide (Fig. 9d).

Therefore, the fault F1 will be overpressurized before a hydraulic connection with the injection source is reached. This over-pressure combined with

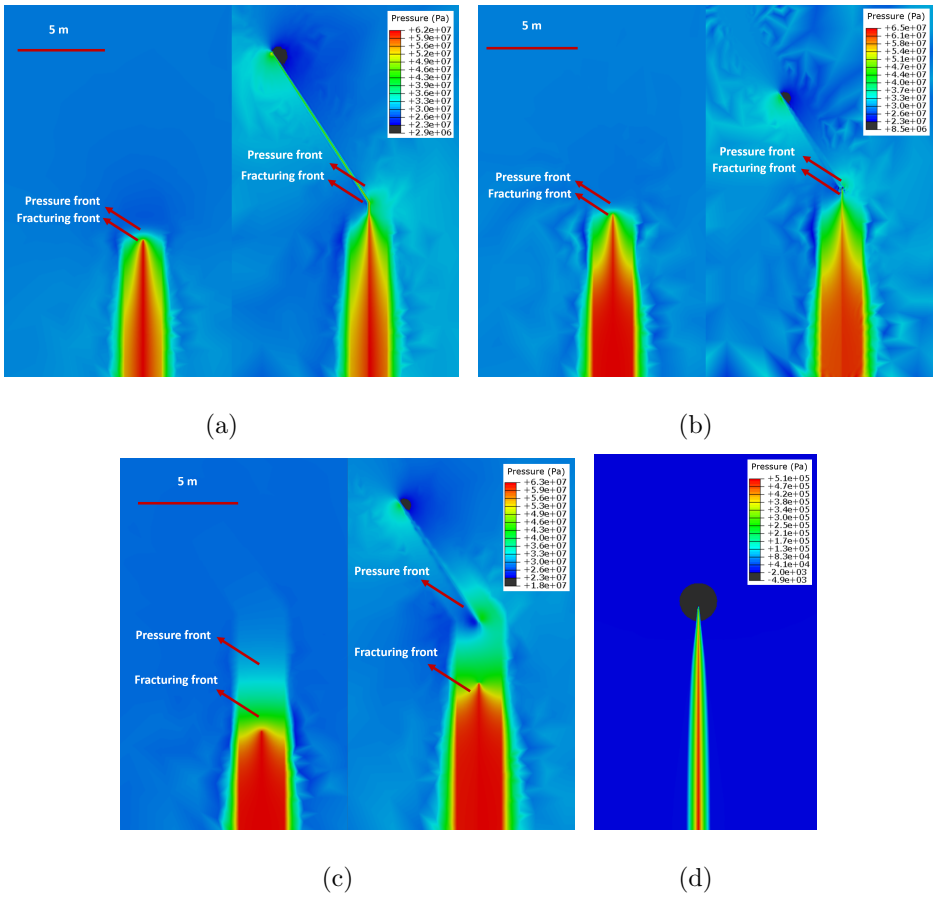

Fig. 9. Hydraulic fracturing front and pressure front propagation. (a) case A2; (b) case A8; (c) case A12; (d) case with no leak-off

poro-elastic stressing results in a reduction of the effective normal stress and induces slip along F1 because the induced shear stress exceeds its shear strength. The time lag of the over-pressurized front and fracturing front for cases A2 and A8 is very small (< 0.1 s) such that the sliding looks more continuous. However, for case A12 with a higher FDZ permeability, this time lag becomes obvious (~ 12 s), and F1 undergoes two distinct slips due to over-pressurization and hydraulic shearing, respectively. During the first slip, the total shear slip and slip rate are smaller than those obtained for case A2 and A8, since the pressure perturbation is lower. During the second slip, there is mainly aseismic slip and this is because most of the accumulated strain energy has been released during the first slip. As a result, the slip and slip rate of F1 exhibit an obvious downward trend as permeability increases (Fig. 10a).

For each tested value for the FDZ permeability, we observed that F2 is activated by the pressure diffusion and poro-elasticity though the activation time differs for each case. A higher permeability requires less fluid injection, i.e., 150 - 160 s for k_{f1} = 1e-15 m^2, 120 - 130 s for k_{f2} = 5e-15 m^2, and only 100 - 110 s for k_{f3} = 1e-14 m^2. When the injection time is identical, the higher the permeability, the shorter the time lag for F2 reactivation. For example, with an injection duration of 160 s, F2 has a quiescence of 360.1 s and 34.7 s after shut-in for case A2 and case A8, whereas it is even activated during the injection for case A12. The permeability has a limited influence on magnitude of resolved slip and its rate of F2, which are around 0.8 mm and 35 mm/s (Fig. 10b), respectively. They are slightly increased with more fluid injection at each permeability.

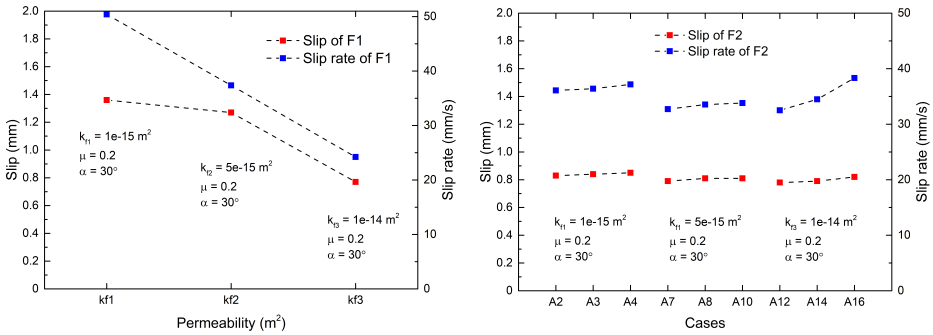

(a) (b)

Fig. 10. Seismic slip and slip rate of (a) F1 and (b) F2 with different permeability in the damage zone

4.2 Friction coefficient

The effect of the friction coefficient on fault slip behavior due to direct injection can be seen from Fig. 11(a), corresponding to cases A2, B1 and B2 in Tab. 3. Triggering by direct fluid injection, faults with a higher friction coefficient tend to display a higher level of slip and higher slip rates. As stated by Ngo et al. (2019), this is because more accumulated energy are required to activate faults with higher friction coefficient, and accordingly more energy is released during slip. In addition, unlike faults with a smaller friction coefficient, which are more likely to be activated by pressure diffusion and poro-elastic stressing before hydraulic shearing, the faults with higher friction coefficient tend to slip only during hydraulic shearing and therefore more violently.

As for the shut-in stage, because F2 cannot be activated with permeability k_f = 1e-15 m^2 in case B1, we keep the friction coefficient of F1 constant as $\mu_1 = 0.2$ and set case A12 as the base case (k_f = 1e-14 m^2). When

the friction coefficient of F2 is 0.4, F2 activation can be observed either by increasing injection duration to 180 s (case B4) or permeability to 1e-13 m^2 (case B5). For $\mu_2 = 0.6$, F2 cannot be triggered unless these two parameters are simultaneously increased (case B7). These illustrate that a higher friction coefficient hinders fault reactivation. However, once F2 slips, higher slip and slip rate are observed when the friction coefficient is larger (Fig. 11(b)), similar to the slip behavior observed during the fluid injection phase.

Table 3. Summary of key parameters and results with different friction coefficient

Case*	**Injection time (s)**	k_f **(m^2)**	μ_1	μ_2	**Slip onset of F1 (s)**	**Slip onset of F2 (s)**
A2	160	1.0e-15	0.2	0.2	38.12	360.1
B1	160	1.0e-15	0.4	0.4	38.12	-
B2	160	1.0e-15	0.6	0.6	38.12	-
A12	160	1.0e-14	0.2	0.2	35.83	150.8 (in)
B3	170	1.0e-14	0.2	0.4	35.83	-
B4	180	1.0e-14	0.2	0.4	35.83	75.7
B5	160	1.0e-13	0.2	0.4	25.62	145.9 (in)
B6	175	1.0e-13	0.2	0.6	25.62	-
B7	180	1.0e-13	0.2	0.6	25.62	10.2

* all cases have fault orientation $\alpha = 30°$, $\mu_1 = 0.2$, injection rate Q = 0.001 m^3/s;

4.3 Fault orientation

On the basis of case A2, we conduct additional simulations where we varied the fault orientation, by changing the fault angle α (tested value are

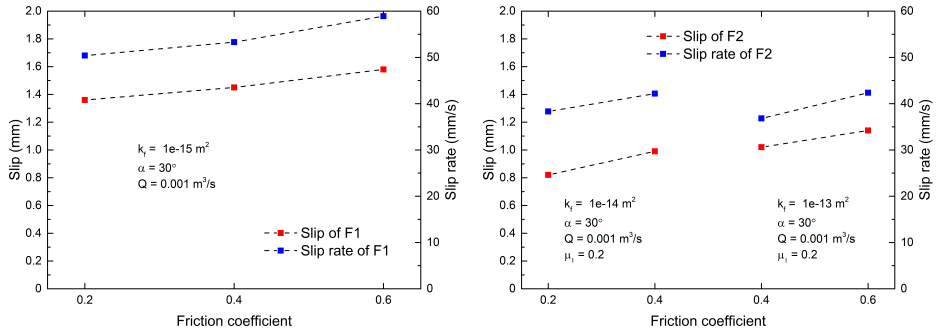

(a) (b)

Fig. 11. Seismic slip and slip rate of (a) F1 and (b) F2 with different friction coefficient

45°, 20° and 10°, see Tab. 4).

During the fluid injection stage, the hydraulic connection of the injection well-bore and the fault F1 occurs at 40.68 s, 39.48 s, 38.12 s, and 35.83 s when the fault angle increases from 10° to 45°, suggesting that a smaller fault dip tends to hinder hydraulic fracture propagation. We infer that this is because the pre-existing fault modifies local stress distributions and the latter depends primarily on the fault orientation. In addition, as the fault dip decreases, the triggered slip and slip rate decrease (Fig. 12(a)), in particular, when the fault angle is 10° (case C4), the slip exhibits mainly aseismic behavior and the averaged slip rate is only about 2.3 mm/s.

During the shut-in stage, except case A2, only case C1 with $\alpha = 45°$ induces F2 activation at 85.7 s after termination in comparison with 360.1 s in case A2. For the 20° model, the shut-in effect of F2 appears when the permeability of FDZ is enhanced from k_{f1} = 1e-15 m^2 to k_{f3} = 1e-14 m^2 (case C3). For the 10° model, F2 can be activated not only with even a higher FDZ permeability (1e-13 m^2), but a higher injection rate 1.6 m^3/s in

case C3 (we will show that a higher injection rate is more likely to trigger shut-in slip in the next section). The results demonstrate that a higher fault orientation is more sensitive to F2 reactivation after shut-in. Furthermore, it tends to induce a larger shear slippage with a higher slip rate (Fig. 12(b)).

Table 4. Summary of key parameters and results with different fault angle

Case*	**Injection time (s)**	k_f **(m^2)**	α **(°)**	**Slip onset of F1 (s)**	**Slip onset of F2 (s)**
A2	160	1.0e-15	30	38.12	360.1
C1	160	1.0e-15	45	35.83	85.7
C2	160	1.0e-15	20	39.48	-
C3	160	1.0e-14	20	40.16	42.2
C4	160	1.0e-15	10	40.68	-
C5	100	1.0e-13	10	35.07	4.0

* all cases have $\mu_1 = \mu_2 = 0.2$, injection rate Q = 0.001 m^3/s except for case C7, which is 0.0016 m^3/s.

4.4 Injection scheme

In this section, we investigate the effect of injection scheme, by considering case A2 as the reference case (Tab. 5).

In a first step, we change the injection rate to 0.0016 m^3/s, 0.0008 m^3/s and 0.0005 m^3/s , corresponding cases E1, E2 and E3 (Fig. 13a), respectively. Worth noting is that we adjust the duration of the injection as to maintain the same injection volume for all experiments. As expected, lowering the injection rate extends the time to reactivate F1. When Q = 0.0016, 0.001 and 0.0008 m^3/s, F2 can be reactivated but with a longer delay at 97.7 s,

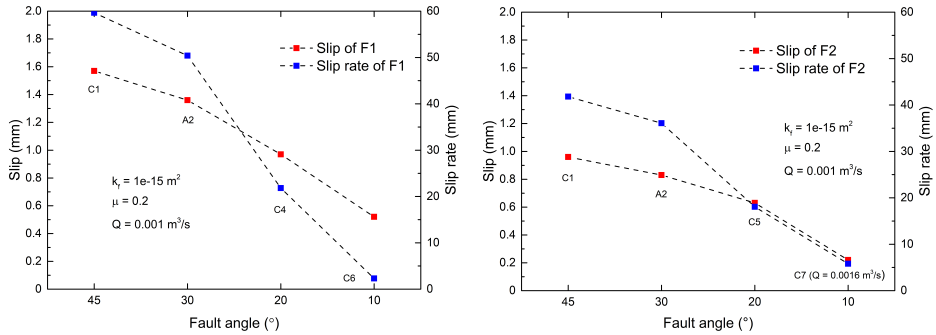

(a) (b)

Fig. 12. Seismic slip and slip rate of (a) F1 and (b) F2 with different fault angle

360.1 s and 410 s after shut-in, respectively. No slip of F2 is observed when the injection rate further reduces to 0.0005 m^3/s. Either during injection or after shut-in, the injection rate has only a limited impact on the total seismic slip, though fault slip rates decrease with decreasing injection rates (Fig. 14), which results in a more stable energy release mode.

In a second stage, we keep the injection rate as constant (0.001 m^3/s), but we change the injection protocol. We consider a step-wise injection schedule (a period of constant injection followed by a pause) by maintaining the same total volume of fluid injected (Fig. 13b).

In case E4, the stimulation is divided evenly into 4 injections and 3 pauses (i.e., a cycling stimulation), each injection/pulse has a duration of 40 s. Since F1 reactivation occurs at 38.12 s $<$ 40 s in case A2, this setting will not change the response of F1 during injection. However, the relaxation of stimulation during the injection favours pressure relaxation, which prevents the reactivation of F2. In case E5, the first injection and suspending time in case E4 are changed to 30 s and 50 s, respectively. In this case, F1 is

activated during the first pause (47.83 s) due to pressure diffusion and poro-elastic stressing, while mainly hydraulic shearing occurs during the second injection (80.27 s). Compared to case E4, not only F2 reactivation after shut-in is prevented in case E5, but the injection-induced slip and slip rate of F1 are significantly reduced owing to the double slip effect, i.e., 1.36 mm and 50.4 mm/s for case E4 vs. 0.75/0.18 mm and 26.97/25.95 mm/s for case E5. It is equivalent to artificially extend the interval between the pressure diffusion and hydraulic shearing, producing a longer and more stable energy release.

Table 5. Summary of key parameters and results with different injection schemes

Case*	**Injection time (s)**	**Injection rate (m^3/s)**	**Slip onset of F1 (s)**	**Slip onset of F2 (s)**
A2	160	0.001	38.12	360.1
E1	100	0.0016	21.85	97.7
E2	200	0.0008	47.24	410.0
E3	320	0.0005	73.17	-
E4	40×4	0.001	38.12	-
E5	30+50+40×2	0.001	47.83/80.27	-

* all cases have k_f =1e-15 m^2, $\mu_1 = \mu_2 = 0.2$, fault orientation $\alpha = 30°$.

5. Discussion

5.1 Comparison with earthquake fault scaling relations

It is well known that unstable fault slip is accompanied by a cluster of induced seismic events (Zoback, 2010; Ellsworth, 2013). To quantify their

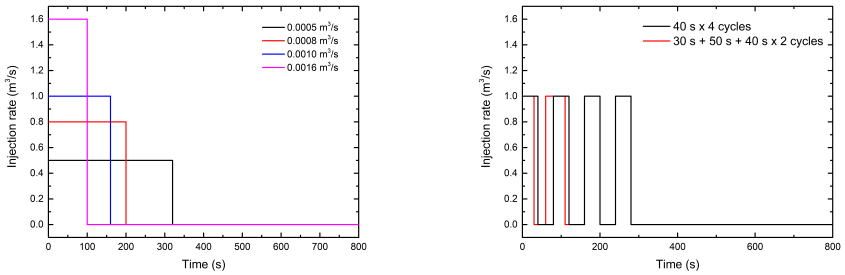

(a) (b)

Fig. 13. Injection scenarios with a constant injection volume: (a) constant injection rate and (b) cyclic injection rate

strength, Aki (1966) first defined the scalar seismic moment M_0 as:

$$M_0 = G\overline{d}A \tag{15}$$

where G is the shear modulus, $\overline{d}$ and A denote the fault shear displacement and fault rupture area, respectively.

The moment magnitude M_w can be then computed by assuming a GR statistics as (Hanks and Kanamori, 1979):

$$M_w = \frac{2}{3}[log_{10}(M_0) - 9.1] \tag{16}$$

where we consider a GR b-value equal to 1 in deriving Eq. (16).

We calculate the moment magnitude for each case based on the obtained seismic slip. Considering that the fault slip occurs during a very short time, we assume that the rupture covers the whole fault, therefore the rupture length is identical to the fault length, and we can approximate the sliding distance as the average seismic slip computed (Lei et al., 2021). For calcu-

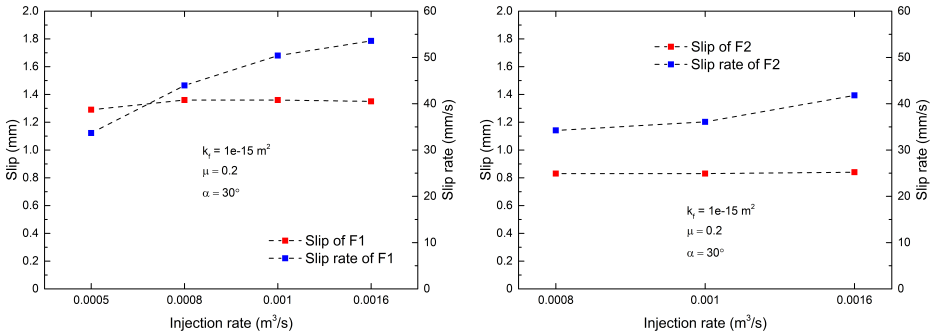

(a) (b)

Fig. 14. Seismic slip and slip rate of (a) F1 and (b) F2 with different injection scenarios

lating the rupture area, we assume that the rupture width is equal to the rupture length, which is supported by a large number of reported earthquakes (Yoon et al., 2017).

We compare the results with two earthquake fault scaling relations. The first one describes the relationship between induced magnitude, fault size, shear slip and stress drop (Zoback and Gorelick, 2012). In our simulations we compute a shear slip between 0.22 and 1.57 mm, corresponding to Mw from -0.39 to 0.18. The related stress drop ranges from 4.29 MPa to 19.79 MPa, suggesting a good consistency with adopted scaling laws (Fig. 15). The second comparison relates the magnitude with the rupture area. Although with a smaller rupture size, our results are still in good agreement with numerous earthquakes (Fig. 16).

5.2 Comparison induced seismicity during injection and after shut-in

Our results show that pre-existing faults can be reactivated and exhibit dynamic slip under certain conditions even faults and hydraulic fractures

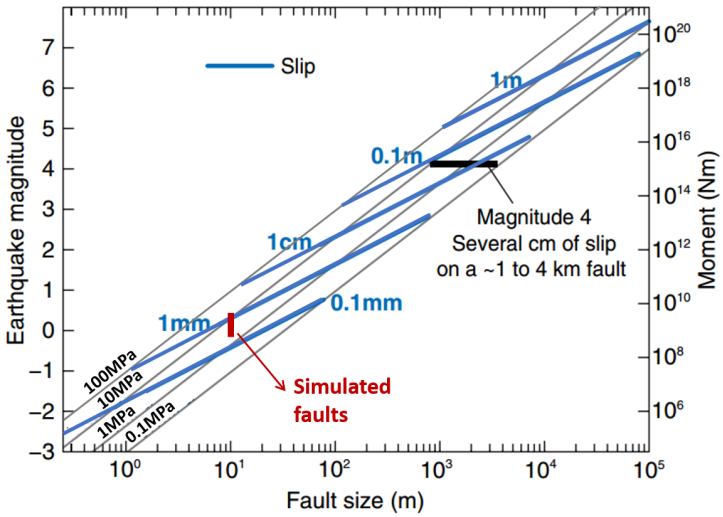

Fig. 15. Earthquake parameters scaling for fault slip, fault size, stress drop and magnitude, modified from (Zoback and Gorelick, 2012)

are non-hydraulically connected, illustrating that seismic events can be induced during the post-injection period triggered by pore pressure diffusion and poro-elastic stress change mechanisms. This is in agreement with field observations as those reported in Soultz-sous-Forêt EGS site (Baisch et al., 2010). In addition, this post-injection reactivation of fault occurs after a period of quiescence, sometimes even exceeding twice of the injection time in our simulations (e.g., case A2 and case E2). This delayed phenomenon has been also observed in other EGS projects as in Rittershoffen (Lengliné et al., 2017).

Most of the cases that display reactivation of F2 after shut-in we note that induced slip and rates computed at F1 during injection are larger than those obtained in F2 during the post injection stage. However, there are also some cases showing an inverse trend, i.e., F2 produces more shear slip and higher

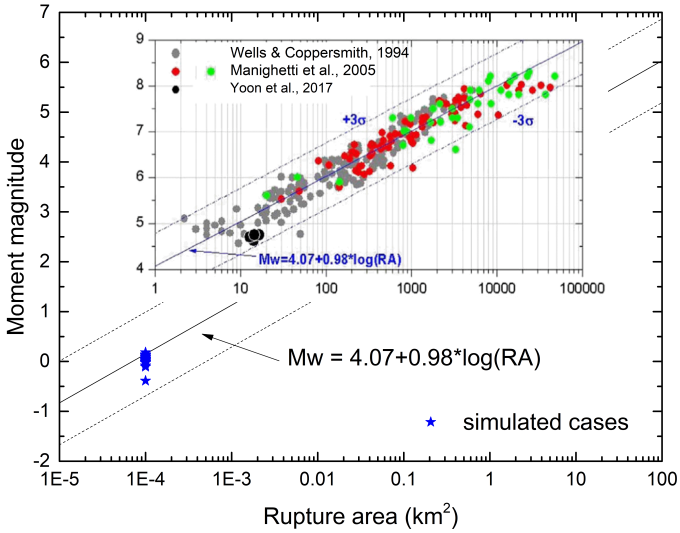

Fig. 16. Moment magnitude as a function of rupture area, modified from (Yoon et al., 2017)

slip rate than F1. We single out these cases and find that they generally share similar conditions, i.e., the diffusivity (permeability) in their nearby regions is extremely high (1e-14 m^2 or 1e-13 m^2), e.g., cases A10 - A12, B3 - B5. In these cases, F1 reactivation due to large pressure gradient occurs earlier than the direct hydraulic shearing, but this pressure disturbance is smaller compared to F2 after shut-in. Thus, the strain energy of F1 is released more evenly than F2. The results may provide an explanation for a common observation in the field, that is that the post injection might induce larger magnitude earthquakes (Häring et al., 2008; Mukuhira et al., 2013). They also shed light on mitigating the risk of fluid induced earthquake. As shown in case E5, which displays double slip events in F1 during active injection, a

lower surrounding permeability (1e-15 m^2) significantly reduces the induced seismic slip and its slip rates. By injecting the same amount of fluid, although cases E5 and E3 both lower the slip of F1 and evade the post-activation of F2, case E5 is more efficient because it consumes less time (280 s vs. 320 s). Therefore, on the basis of our analysis, we can conclude that a soft cycling stimulation strategy might be effective in controlling fluid injection induced seismicity, as suggested by (Hofmann et al., 2018; Zang et al., 2019; Zhuang et al., 2019).

Our results also suggest that the permeability beyond the stimulated zone is of great importance for the shut-in phase. After shut-in, high pressure in the stimulated region diffuses to the surrounding porous matrix, and coupled to induced poro-elastic stress changes can lead to activation of F2 and induced seismicity, thereby extending the seismic region. The work of McClure (2015) showed that the fluid pressure is redistributed and pressure front progresses further after shut-in, extending the pressurized area and induces seismicity. Mukuhira et al. (2017) studied the behavior of pore pressure migration at shut-in phase in Basel and pointed out that large events tend to occur in regions with enhanced permeability. In our case, we set large permeability outside the stimulated region, causing pore pressure to migrate far field the seismic zone after termination.

5.3 The role of initial stress state

Our parametric study shows that there are multiple factors affecting fault slip behavior both during injection and after shut-in. For example, higher permeability reduces the seismic slip but more via double slip effect during the injection period and has little impact on the induced fault slip during

the shut-in stage (Fig. 10), and the soft cycle injection lowers the seismic slip rate effectively (Fig. 14). In contrast, the fault orientation seems to have the greatest influence on the fault slip. As shown in Fig. 12, when the fault angle decreases, the seismic slip and slip rate drop significantly and the faults tend to slip aseismically regardless if during injection or after shut-in. This may be related to the initial stress state of the faults. To evaluate the initial potential for fault reactivation, we calculate the slip tendency ST, which is defined as the ratio between the absolute shear stress and effective normal stress (Blöcher et al., 2018):

$$\mathrm{ST} = \frac{|\tau|}{|\sigma_n'|} \tag{17}$$

The initial shear stress and effective normal stress of fault are given by (Jaeger et al., 2009):

$$\tau = \frac{\sigma_1 - \sigma_3}{2}\sin(2\alpha) \tag{18}$$

$$\sigma_n' = \frac{\sigma_1' + \sigma_3'}{2} + \frac{\sigma_1' - \sigma_3'}{2}\cos(2\alpha) \tag{19}$$

At the given initial stress state (Tab. 1), the slip tendency ST = 0.034, 0.069, 0.096, 0.108 for the fault angle $\alpha = 10°$, $20°$, $30°$ and $45°$, suggesting an increasing critical condition for fault reactivation. Moreover, a larger initial slip tendency leads to higher seismic slip and slip rate under the same perturbation (see Fig. 12). To further validate this hypothesis, we conduct another simulation by only reducing the minimum principal stress σ_3 from 29 MPa to 24 MPa from case A2. Accordingly, the initial slip tendency increases from a nominal value of 0.096 to 0.155, approaching further to the static friction coefficient (0.2). The results show that with only 8.05 s and

28.2 s fluid injection, F1 and F2 are both activated by coupled fluid pressure diffusion and poro-elastic stressing. This is consistent with the main conclusions derived in the study by Lee et al. (2019), where they analyzed induced seismicity in Pohang EGS project and found that the fault which is responsible for the earthquake, was critically stressed, susceptible to slip and very sensitive to even small perturbations. Furthermore, the slip rates of F1 and F2 also increases (mainly due to poro-elastic stressing since F1 slips aseismically when it connects the injection point at 16.87 s), indicating much stronger energy releases. This has important implications for controlling fluid injection-induced seismicity, in particular for post-injection induced seismicity targeting far-field faults. As suggested by (Baisch et al., 2010), post-event magnitude is predominantly affected by the fault geometry and fluid pressure elevation brings stress conditions close to critical values. Mukuhira et al. (2013, 2017) also demonstrated that even a minor increase in pore pressure was sufficient to initiate shear slip and trigger large events at large differential stress. Indeed, many researches even stated that the initial stress controls the nature of the fluid induced seismicity (Yoon et al., 2017; Cappa et al., 2018; Passelègue et al., 2020). This may also be one aspect to get an insight into an observation that a field area of little natural seismicity may have a lower propensity to produce felt or damaging earthquakes (Evans et al., 2012). Therefore, to mitigate the unwanted seismicity, a good prior knowledge of the crust before treatment is required.

6. Conclusion

In this study, we conducted a coupled hydraulic-mechanical numerical model to investigate the induced fault slip behavior during injection and after shut-in. It shows the capability of generating seismic slip either owing to direct hydraulic shearing or fluid pressure diffusion coupled with poro-elastic stressing when there is no connection between the hydraulic fracture and the pre-existing fault.

Through parametric study, we found that fault seismic slip can be attributed to the combined effect of multiple factors but with different emphases. Permeability along the fracture path is of great importance not only for the after shut-in stage, but also for the fracturing process. It allows fluid pressure diffusion induced poro-elastic stress change to activate the fault before the hydraulic shearing. This averages the strain energy release and lowers the seismicity magnitude during injection, providing an explanation for the occurrence of larger earthquakes after shut-in. It also highlights the effectiveness of soft cyclic injection since the fault strain energy can be partly released during each relaxation. Moreover, although the larger friction coefficient favors fault slip and the soft injection can alleviate the slip, the impact of fault orientation on the slip is more dominant. Finally, the combined effect of these factors can be largely attributed to the initial slip tendency and hence the initial stress state. We confirmed that critically-stressed faults are more likely to produce larger shear slip even with only small perturbations. Our results show good consistency with some field observations and previous studies, which have important implications for mitigating fluid injection induced seismicity. In the next step, the influence of fracture networks will

be considered.

Declaration of Competing Interest

The authors declare that they have no known competing financial interests or personal relationships that could have appeared to influence the work reported in this paper.

Acknowledgements

This work was supported by the China Scholarship Council (CSC) [grant number 201808510128].

Appendix A: Validation of the hydraulic fracture propagation

For any complex numerical models involve hydraulic fracture simulation, Lecampion et al. (2018) emphasized the necessity of verification against those analytical solutions. Here the KGD (Kristianovic-Geerstma-de Klerk) model for plane strain hydraulic fracture is selected for validation (Garagash, 2006).

The scaling solutions for the hydraulic aperture w, the average net pressure p, and the fracture length l are given by (Detournay, 2004):

$$\begin{cases} w = \varepsilon(t) \cdot L(t)\Omega[x', P(t)] \\ p = \varepsilon(t) \cdot E'\Pi[x', P(t)] \\ l(t) = L(t) \cdot \gamma[P(t)] \end{cases} \tag{A.1}$$

where $x' = x/l(t)$ is the scaled coordinate, $0 \leq x' \leq 1$. $\varepsilon(t)$, $L(t)$, $P(t)$ denotes a small dimensionless parameter, a length scale if the same order as the fracture length l, and a dimensionless evolution parameter, respectively.

The hydraulic fracture propagation is controlled by either toughness-dominated regime (κ-regime) or viscosity-regime (M-regime) (Carrier and Granet, 2012). The dimensionless viscosity M and toughness κ is given by:

$$M = \kappa^{-4} = \mu' \frac{E'^3 Q_0}{K'^4} \tag{A.2}$$

where $\mu' = 12\mu$; $E' = \dfrac{E}{1-v^2}$; $K' = 4\left(\dfrac{2}{\pi}\right)^{1/2} K_{IC}$.

The toughness scaling is most appropriate for cases when the viscosity scaling M is small. The asymptotic solution $\overline{F}_k(\overline{\Omega}_k, \Pi_k, \gamma_k)$ is given by:

$$\overline{F}_k = \overline{F}_{k_0} + M\overline{F}_{k_1} \tag{A.3}$$

where $\overline{F}_{k_0}(\overline{\Omega}_{k_0}, \Pi_{k_0}, \gamma_{k_0})$ is the zero-viscosity solution given by:

$$\begin{cases} \Omega_{k_0} = \dfrac{\pi^{1/3}}{2}(1-x'^2)^{1/2} \\ \Pi_{k_0} = \dfrac{\pi^{1/3}}{8} \\ \gamma_{k_0} = \dfrac{2}{\pi^{2/3}} \end{cases} \tag{A.4}$$

and the next term $\overline{F}_{k_1}(\overline{\Omega}_{k_1}, \Pi_{k_1}, \gamma_{k_1})$ is:

$$\begin{cases} \Pi_{k_1} = \Pi^*_{k_1} + \Delta\Pi_{k_1} \\ \Omega_{k_1} = 4\Pi^*_{k_1}(1-x'^2)^{1/2} + \dfrac{2}{\pi}\displaystyle\int_0^1 f(x',x)\Delta\Pi_{k_1}(x)\,\mathrm{d}x \\ \gamma_{k_1} \simeq -2.72 \end{cases} \tag{A.5}$$

where

$$\Delta\Pi_{k_1}(x) = \frac{4}{3\pi^{2/3}}\ln(1-x'^2) - \frac{2x'\arccos x'}{\pi^{2/3}(1-x'^2)^{1/2}} \tag{A.6}$$

$$f(x',x) = -\frac{4}{\pi}\ln\left|\frac{\sqrt{1-x'^2}+\sqrt{1-x^2}}{\sqrt{1-x'^2}-\sqrt{1-x^2}}\right| \tag{A.7}$$

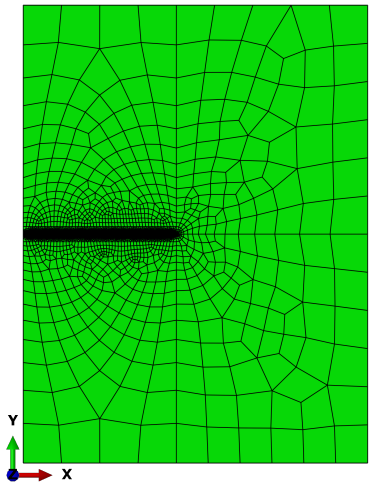

Fig. A.1. Geometry and mesh of the KGD model

For the toughness scaling,

$$\begin{cases} \varepsilon_k = \left(\dfrac{K'^4}{E'^4 Q_0 t}\right)^{1/3} \\ L_k = \left(\dfrac{E' Q_0 t}{K'}\right)^{2/3} \end{cases} \tag{A.8}$$

Fig. A.1 shows the geometry and mesh used in the simulation. Here the 2D model has a dimension 45 m $\times$ 60 m, with a predefined hydraulic fracture path at the middle along the x-axis, simulated by cohesive elements with pore pressure degree of freedom. The well-bore is simplified to be a point and the point injection rate Q is assumed to be constant. Note that only half of the space is simulated due to geometric symmetry.

For cohesive elements, the coarse mesh density may reduce the accuracy (Zielonka et al., 2014). Here we use a finer mesh (the smallest mesh size around the hydraulic fracture path is 0.5 cm) to circumvent this effect (Turon et al., 2007; Ngo et al., 2019). All material parameters used in the simulation

Table A.1. Input material properties for the KGD model

Property	**Symbol**	**Value**	**Unit**
Young's modulus	E	17	GPa
Poisson ratio	v	0.2	-
Fracture Energy	G_c	120	Pa·m
Tensile strength	τ_c	1.25	MPa
Biot's coefficient	b	0.75	-
Biot's Modulus	M_b	68.7	MPa
Permeability	k	1.0e-16	m^2
Porosity	ϕ	0.2	-
Fluid viscosity	η	0.0001	Pa·s
Injection rate	Q	0.001	$m^3 \cdot s^{-1}$

are given in Tab. A.1. According to Eq. (A.2), we obtain $M = 0.0142$, indicating the toughness-dominated regime.

In this simulation, we perform 20 s of hydraulic stimulation. The fracture length, fracture aperture and pressure at the injection point, and the corresponding relative errors are given in Fig. A.2. Results show a good agreement between our numerical results and the analytical solutions except that the numerically obtained injection pressure has an increasing error as time increases. This is due to poro-elastic coupling effect (Carrier and Granet, 2012), which is not considered in the analytical model.

References

Aki, K., 1966. Generation and propagation of g waves from the niigata earthquake of june 16, 1964.: Part 2. estimation of earthquake moment,

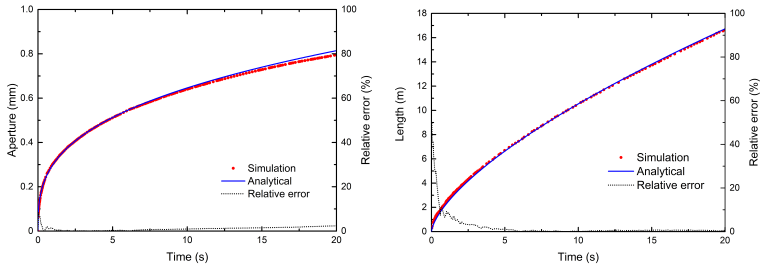

(a) fracture aperture at injection point

(b) fracture length

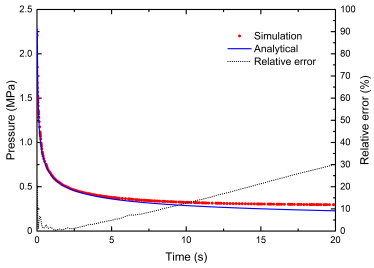

(c) pressure at injection point

Fig. A.2. Comparison between analytical solutions and numerical simulations and the relative error

released energy, and stress-strain drop from the g wave spectrum. Bulletin of the Earthquake Research Institute, University of Tokyo 44, 73–88. URL: `https://ci.nii.ac.jp/naid/120000871042/en/`.

Albaric, J., Oye, V., Langet, N., Hasting, M., Lecomte, I., Iranpour, K., Messeiller, M., Reid, P., 2014. Monitoring of induced seismicity during the first geothermal reservoir stimulation at paralana, australia. Geothermics 52, 120–131. doi:10.1016/j.geothermics.2013.10.013.

Baisch, S., Vörös, R., Rothert, E., Stang, H., Jung, R., Schellschmidt, R., 2010. A numerical model for fluid injection induced seismicity at soultz-

sous-forêts. International Journal of Rock Mechanics and Mining Sciences 47, 405–413. doi:10.1016/j.ijrmms.2009.10.001.

Barati, R., Liang, J.T., 2014. A review of fracturing fluid systems used for hydraulic fracturing of oil and gas wells. Journal of Applied Polymer Science 131. doi:10.1002/app.40735.

Barth, A., Wenzel, F., Langenbruch, C., 2013. Probability of earthquake occurrence and magnitude estimation in the post shut-in phase of geothermal projects. Journal of seismology 17, 5–11. doi:10.1007/s10950-011-9260-9.

Baujard, C., Genter, A., Dalmais, E., Maurer, V., Hehn, R., Rosillette, R., Vidal, J., Schmittbuhl, J., 2017. Hydrothermal characterization of wells grt-1 and grt-2 in rittershoffen, france: Implications on the understanding of natural flow systems in the rhine graben. Geothermics 65, 255–268. doi:10.1016/j.geothermics.2016.11.001.

Biot, M.A., 1941. General theory of three-dimensional consolidation. Journal of applied physics 12, 155–164. doi:10.1063/1.1712886.

Blöcher, G., Cacace, M., Jacquey, A.B., Zang, A., Heidbach, O., Hofmann, H., Kluge, C., Zimmermann, G., 2018. Evaluating micro-seismic events triggered by reservoir operations at the geothermal site of groß schönebeck (germany). Rock Mechanics and Rock Engineering 51, 3265–3279. doi:10.1007/s00603-018-1521-2.

Brown, M.R., Ge, S., 2018. Small earthquakes matter in injection-induced seismicity. Geophysical Research Letters 45, 5445–5453. doi:10.1029/2018GL077472.

Brudzinski, M.R., Kozłowska, M., 2019. Seismicity induced by hydraulic fracturing and wastewater disposal in the appalachian basin, usa: A review. Acta Geophysica 67, 351–364. doi:10.1007/s11600-019-00249-7.

Cappa, F., Guglielmi, Y., Nussbaum, C., Birkholzer, J., 2018. On the relationship between fault permeability increases, induced stress perturbation, and the growth of aseismic slip during fluid injection. Geophysical Research Letters 45, 11–012. doi:10.1029/2018GL080233.

Carrier, B., Granet, S., 2012. Numerical modeling of hydraulic fracture problem in permeable medium using cohesive zone model. Engineering fracture mechanics 79, 312–328. doi:10.1016/j.engfracmech.2011.11.012.

Chang, K., Segall, P., 2016. Injection-induced seismicity on basement faults including poroelastic stressing. Journal of Geophysical Research: Solid Earth 121, 2708–2726. doi:10.1002/2015JB012561.

Chang, K.W., Yoon, H., Martinez, M.J., 2018. Seismicity rate surge on faults after shut-in: Poroelastic response to fluid injection. Bulletin of the Seismological Society of America 108, 1889–1904. doi:10.1785/0120180054.

Chen, Z., Jeffrey, R.G., Zhang, X., Kear, J., et al., 2017. Finite-element simulation of a hydraulic fracture interacting with a natural fracture. Spe Journal 22, 219–234. doi:10.2118/176970-PA.

Colmenares, L.B., Zoback, M.D., 2007. Hydraulic fracturing and wellbore completion of coalbed methane wells in the powder river basin, wyoming: implications for water and gas production. AAPG bulletin 91, 51–67. doi:10.1306/07180605154.

Cornet, F., Jianmin, Y., 1995. Analysis of induced seismicity for stress field determination and pore pressure mapping, in: Mechanics Problems in Geodynamics Part I. Springer, pp. 677–700.

Coussy, O., 2004. Poromechanics. John Wiley & Sons.

De Barros, L., Cappa, F., Guglielmi, Y., Duboeuf, L., Grasso, J.R., 2019. Energy of injection-induced seismicity predicted from in-situ experiments. Scientific reports 9, 1–11. doi:10.1038/s41598-019-41306-x.

De Simone, S., Carrera, J., Vilarrasa, V., 2017. Superposition approach to understand triggering mechanisms of post-injection induced seismicity. Geothermics 70, 85–97. doi:10.1016/j.geothermics.2017.05.011.

Deng, Q., Blöcher, G., Cacace, M., Schmittbuhl, J., 2021. Hydraulic diffusivity of a partially open rough fracture. Rock Mechanics and Rock Engineering , 1–23.

Detournay, E., 2004. Propagation regimes of fluid-driven fractures in impermeable rocks. International Journal of Geomechanics 4, 35–45. doi:10.1061/(ASCE)1532-3641(2004)4:1(35).

Ellsworth, W.L., 2013. Injection-induced earthquakes. Science 341, 1225942. doi:10.1126/science.1225942.

Evans, J.P., Forster, C.B., Goddard, J.V., 1997. Permeability of fault-related rocks, and implications for hydraulic structure of fault zones. Journal of structural Geology 19, 1393–1404. doi:10.1016/S0191-8141(97)00057-6.

Evans, K.F., Moriya, H., Niitsuma, H., Jones, R., Phillips, W., Genter, A., Sausse, J., Jung, R., Baria, R., 2005. Microseismicity and permeability enhancement of hydrogeologic structures during massive fluid injections into granite at 3 km depth at the soultz hdr site. Geophysical Journal International 160, 388–412. doi:10.1111/j.1365-246X.2004.02474.x.

Evans, K.F., Zappone, A., Kraft, T., Deichmann, N., Moia, F., 2012. A survey of the induced seismic responses to fluid injection in geothermal and co2 reservoirs in europe. Geothermics 41, 30–54. doi:10.1016/j.geothermics.2011.08.002.

Fehler, M.C., 1989. Stress control of seismicity patterns observed during hydraulic fracturing experiments at the fenton hill hot dry rock geothermal energy site, new mexico, in: International Journal of Rock Mechanics and Mining Sciences & Geomechanics Abstracts, Elsevier. pp. 211–219. doi:10.1016/0148-9062(89)91971-2.

Garagash, D.I., 2006. Plane-strain propagation of a fluid-driven fracture during injection and shut-in: Asymptotics of large toughness. Engineering fracture mechanics 73, 456–481. doi:10.1016/j.engfracmech.2005.07.012.

Gaucher, E., Schoenball, M., Heidbach, O., Zang, A., Fokker, P., van Wees, J.D., Kohl, T., 2015. Induced seismicity in geothermal reservoirs: physical processes and key parameters, in: World Geothermal Congress 2015.

Gu, H., Weng, X., Lund, J.B., Mack, M.G., Ganguly, U., Suarez-Rivera, R., et al., 2012. Hydraulic fracture crossing natural fracture at nonorthogonal

angles: a criterion and its validation. SPE Production & Operations 27, 20–26. doi:10.2118/139984-PA.

Guglielmi, Y., Cappa, F., Avouac, J.P., Henry, P., Elsworth, D., 2015. Seismicity triggered by fluid injection–induced aseismic slip. Science 348, 1224–1226. doi:10.1126/science.aab0476.

Hanks, T.C., Kanamori, H., 1979. A moment magnitude scale. Journal of Geophysical Research: Solid Earth 84, 2348–2350. doi:10.1029/JB084iB05p02348.

Häring, M.O., Schanz, U., Ladner, F., Dyer, B.C., 2008. Characterisation of the basel 1 enhanced geothermal system. Geothermics 37, 469–495. doi:10.1016/j.geothermics.2008.06.002.

Hearn, E.H., Koltermann, C., Rubinstein, J.L., 2018. Numerical models of pore pressure and stress changes along basement faults due to wastewater injection: Applications to the 2014 milan, kansas earthquake. Geochemistry, Geophysics, Geosystems 19, 1178–1198. doi:10.1002/2017GC007194.

Hofmann, H., Zimmermann, G., Zang, A., Min, K.B., 2018. Cyclic soft stimulation (css): a new fluid injection protocol and traffic light system to mitigate seismic risks of hydraulic stimulation treatments. Geothermal Energy 6, 27. doi:10.1186/s40517-018-0114-3.

Howard, G.C., Fast, C., 1957. Optimum fluid characteristics for fracture extension, in: Drilling and production practice, OnePetro.

Hsieh, P.A., Bredehoeft, J.D., 1981. A reservoir analysis of the denver earthquakes: A case of induced seismicity. Journal of Geophysical Research: Solid Earth 86, 903–920. doi:10.1029/JB086iB02p00903.

Jacquey, A.B., Urpi, L., Cacace, M., Blöcher, G., Zimmermann, G., Scheck-Wenderoth, M., 2018. Far field poroelastic response of geothermal reservoirs to hydraulic stimulation treatment: Theory and application at the groß schönebeck geothermal research facility. International Journal of Rock Mechanics and Mining Sciences 110, 316–327. doi:10.1016/j.ijrmms.2018.08.012.

Jaeger, J.C., Cook, N.G., Zimmerman, R., 2009. Fundamentals of rock mechanics. John Wiley & Sons.

Ji, Y., Wu, W., Zhao, Z., 2019. Unloading-induced rock fracture activation and maximum seismic moment prediction. Engineering Geology 262, 105352. doi:10.1016/j.enggeo.2019.105352.

Johri, M., Zoback, M.D., 2013. The evolution of stimulated reservoir volume during hydraulic stimulation of shale gas formations, in: Unconventional Resources Technology Conference, Society of Exploration Geophysicists, American Association of Petroleum .... pp. 1661–1671. doi:10.1190/urtec2013-170.

Keranen, K.M., Weingarten, M., Abers, G.A., Bekins, B.A., Ge, S., 2014. Sharp increase in central oklahoma seismicity since 2008 induced by massive wastewater injection. Science 345, 448–451. doi:10.1126/science.1255802.

Kettlety, T., Verdon, J., Werner, M., Kendall, J., 2020. Stress transfer from opening hydraulic fractures controls the distribution of induced seismicity. Journal of Geophysical Research: Solid Earth 125, e2019JB018794. doi:10.1029/2019JB018794.

Krietsch, H., Villiger, L., Doetsch, J., Gischig, V., Evans, K.F., Brixel, B., Jalali, M., Loew, S., Giardini, D., Amann, F., 2020. Changing flow paths caused by simultaneous shearing and fracturing observed during hydraulic stimulation. Geophysical Research Letters 47, e2019GL086135. doi:10.1029/2019GL086135.

Langenbruch, C., Weingarten, M., Zoback, M.D., 2018. Physics-based forecasting of man-made earthquake hazards in oklahoma and kansas. Nature communications 9, 1–10. doi:10.1038/s41467-018-06167-4.

Law, B.E., Spencer, C.W., Howell, D., Wiese, K., Fanelli, M., Zink, L., Cole, F., 1993. Gas in tight reservoirs—an emerging major source of energy. US Geological Survey Professional Paper 1570, 233–252. URL: `https://www.osti.gov/biblio/6814307`.

Lecampion, B., Bunger, A., Zhang, X., 2018. Numerical methods for hydraulic fracture propagation: a review of recent trends. Journal of natural gas science and engineering 49, 66–83. doi:10.1016/j.jngse.2017.10.012.

Lee, K.K., Ellsworth, W.L., Giardini, D., Townend, J., Ge, S., Shimamoto, T., Yeo, I.W., Kang, T.S., Rhie, J., Sheen, D.H., et al., 2019. Managing injection-induced seismic risks. Science 364, 730–732. doi:10.1126/science.aax1878.

Lei, Q., Doonechaly, N.G., Tsang, C.F., 2021. Modelling fluid injection-induced fracture activation, damage growth, seismicity occurrence and connectivity change in naturally fractured rocks. International Journal of Rock Mechanics and Mining Sciences 138, 104598. doi:10.1016/j.ijrmms.2020.104598.

Lei, X., Huang, D., Su, J., Jiang, G., Wang, X., Wang, H., Guo, X., Fu, H., 2017. Fault reactivation and earthquakes with magnitudes of up to mw4. 7 induced by shale-gas hydraulic fracturing in sichuan basin, china. Scientific reports 7, 1–12. doi:10.1038/s41598-017-08557-y.

Lei, X., Wang, Z., Su, J., 2019. The december 2018 ml 5.7 and january 2019 ml 5.3 earthquakes in south sichuan basin induced by shale gas hydraulic fracturing. Seismological Research Letters 90, 1099–1110. doi:10.1785/0220190029.

Lengliné, O., Boubacar, M., Schmittbuhl, J., 2017. Seismicity related to the hydraulic stimulation of grt1, rittershoffen, france. Geophysical Journal International 208, 1704–1715. doi:10.1093/gji/ggw490.

Li, Y., Deng, J., Liu, W., Feng, Y., 2017. Modeling hydraulic fracture propagation using cohesive zone model equipped with frictional contact capability. Computers and geotechnics 91, 58–70. doi:10.1016/j.compgeo.2017.07.001.

Liu, Y., Guo, J., Chen, Z., 2016. Leakoff characteristics and an equivalent leakoff coefficient in fractured tight gas reservoirs. Journal of Natural Gas Science and Engineering 31, 603–611.

Majer, E.L., Baria, R., Stark, M., Oates, S., Bommer, J., Smith, B., Asanuma, H., 2007. Induced seismicity associated with enhanced geothermal systems. Geothermics 36, 185–222. doi:10.1016/j.geothermics.2007.03.003.

Maurer, J., Dunham, E.M., Segall, P., 2020. Role of fluid injection on earthquake size in dynamic rupture simulations on rough faults. Geophysical Research Letters 47, e2020GL088377. doi:10.1029/2020GL088377.

McClure, M.W., 2015. Generation of large postinjection-induced seismic events by backflow from dead-end faults and fractures. Geophysical Research Letters 42, 6647–6654. doi:10.1002/2015GL065028.

McClure, M.W., Horne, R.N., 2011. Investigation of injection-induced seismicity using a coupled fluid flow and rate/state friction model. Geophysics 76, WC181–WC198. doi:10.1190/geo2011-0064.1.

McDaniel, B., et al., 1990. Hydraulic fracturing techniques used for stimulation of coalbed methane wells, in: SPE Eastern Regional Meeting, Society of Petroleum Engineers. doi:10.2118/21292-MS.

Meyer, G., Baujard, C., Hehn, R., Genter, A., McClure, M., 2017. Analysis and numerical modelling of pressure drops observed during hydraulic stimulation of grt-1 geothermal well (rittershoffen, france). Proc 42nd Work Geotherm Reserv Eng , 14.

Mitchell, T., Faulkner, D., 2012. Towards quantifying the matrix permeability of fault damage zones in low porosity rocks. Earth and Planetary Science Letters 339, 24–31. doi:10.1016/j.epsl.2012.05.014.

Mukuhira, Y., Asanuma, H., Niitsuma, H., Häring, M.O., 2013. Characteristics of large-magnitude microseismic events recorded during and after stimulation of a geothermal reservoir at basel, switzerland. Geothermics 45, 1–17. doi:10.1016/j.geothermics.2012.07.005.

Mukuhira, Y., Dinske, C., Asanuma, H., Ito, T., Häring, M., 2017. Pore pressure behavior at the shut-in phase and causality of large induced seismicity at basel, switzerland. Journal of Geophysical Research: Solid Earth 122, 411–435. doi:10.1002/2016JB013338.

Murphy, H., Brown, D., Jung, R., Matsunaga, I., Parker, R., 1999. Hydraulics and well testing of engineered geothermal reservoirs. Geothermics 28, 491–506. doi:10.1016/S0375-6505(99)00025-5.

Nara, Y., Meredith, P.G., Yoneda, T., Kaneko, K., 2011. Influence of macro-fractures and micro-fractures on permeability and elastic wave velocities in basalt at elevated pressure. Tectonophysics 503, 52–59. doi:10.1016/j.tecto.2010.09.027.

Ngo, D.T., Pellet, F.L., Bruel, D., 2019. Modeling of fault slip during hydraulic stimulation in a naturally fractured medium. Geomechanics and Geophysics for Geo-Energy and Geo-Resources 5, 237–251. doi:10.1007/s40948-019-00108-1.

Norbeck, J.H., McClure, M.W., Horne, R.N., 2018. Field observations at the fenton hill enhanced geothermal system test site support mixed-mechanism stimulation. Geothermics 74, 135–149. doi:10.1016/j.geothermics.2018.03.003.

Norbeck, J.H., McClure, M.W., Lo, J.W., Horne, R.N., 2016. An embedded fracture modeling framework for simulation of hydraulic fracturing and shear stimulation. Computational Geosciences 20, 1–18. doi:10.1007/s10596-015-9543-2.

Parotidis, M., Shapiro, S.A., Rothert, E., 2004. Back front of seismicity induced after termination of borehole fluid injection. Geophysical Research Letters 31. doi:10.1029/2003GL018987.

Passelègue, F.X., Almakari, M., Dublanchet, P., Barras, F., Fortin, J., Violay, M., 2020. Initial effective stress controls the nature of earthquakes. Nature communications 11, 1–8. doi:10.1038/s41467-020-18937-0.

Passelègue, F.X., Brantut, N., Mitchell, T.M., 2018. Fault reactivation by fluid injection: controls from stress state and injection rate. Geophysical Research Letters 45, 12–837. doi:10.1029/2018GL080470.

Pearson, C., 1981. The relationship between microseismicity and high pore pressures during hydraulic stimulation experiments in low permeability granitic rocks. Journal of Geophysical Research: Solid Earth 86, 7855–7864. doi:10.1029/JB086iB09p07855.

Piris, G., Griera, A., Gomez-Rivas, E., Herms, I., McClure, M.W., Norbeck, J.H., 2018. Fluid pressure drops during stimulation of segmented faults in deep geothermal reservoirs. Geothermal Energy 6, 24. doi:10.1186/s40517-018-0110-7.

Ren, L., Lin, R., Zhao, J.z., Yang, K.w., Hu, Y.q., Wang, X.j., 2015. Simultaneous hydraulic fracturing of ultra-low permeability sandstone reservoirs

in china: Mechanism and its field test. Journal of Central South University 22, 1427–1436. doi:10.1007/s11771-015-2660-1.

Rutqvist, J., Rinaldi, A.P., Cappa, F., Moridis, G.J., 2013. Modeling of fault reactivation and induced seismicity during hydraulic fracturing of shale-gas reservoirs. Journal of Petroleum Science and Engineering 107, 31–44. doi:10.1016/j.petrol.2013.04.023.

Saadat, M., Taheri, A., 2019. A cohesive discrete element based approach to characterizing the shear behavior of cohesive soil and clay-infilled rock joints. Computers and Geotechnics 114, 103109. doi:10.1016/j.compgeo.2019.103109.

Schill, E., Genter, A., Cuenot, N., Kohl, T., 2017. Hydraulic performance history at the soultz egs reservoirs from stimulation and long-term circulation tests. Geothermics 70, 110–124. doi:10.1016/j.geothermics.2017.06.003.

Shapiro, S.A., Audigane, P., Royer, J.J., 1999. Large-scale in situ permeability tensor of rocks from induced microseismicity. Geophysical Journal International 137, 207–213. doi:10.1046/j.1365-246x.1999.00781.x.

Stanchits, S., Mayr, S., Shapiro, S., Dresen, G., 2011. Fracturing of porous rock induced by fluid injection. Tectonophysics 503, 129–145. doi:10.1016/j.tecto.2010.09.022.

Turon, A., Davila, C.G., Camanho, P.P., Costa, J., 2007. An engineering solution for mesh size effects in the simulation of delamination using cohesive zone models. Engineering fracture mechanics 74, 1665–1682. doi:10.1016/j.engfracmech.2006.08.025.

Ucar, E., Berre, I., Keilegavlen, E., 2017. Postinjection normal closure of fractures as a mechanism for induced seismicity. Geophysical Research Letters 44, 9598–9606. doi:10.1002/2017GL074282.

Wang, J., Elsworth, D., Denison, M.K., 2018. Hydraulic fracturing with leakoff in a pressure-sensitive dual porosity medium. International Journal of Rock Mechanics and Mining Sciences 107, 55–68. doi:10.1016/j.ijrmms.2018.04.042.

Wang, L., Kwiatek, G., Rybacki, E., Bohnhoff, M., Dresen, G., 2020. Injection-induced seismic moment release and laboratory fault slip: Implications for fluid-induced seismicity. Geophysical Research Letters 47, e2020GL089576. doi:10.1029/2020GL089576.

Xie, L., Min, K.B., 2016. Initiation and propagation of fracture shearing during hydraulic stimulation in enhanced geothermal system. Geothermics 59, 107–120. doi:10.1016/j.geothermics.2015.10.012.

Yao, Y., 2012. Linear elastic and cohesive fracture analysis to model hydraulic fracture in brittle and ductile rocks. Rock mechanics and rock engineering 45, 375–387. doi:10.1007/s00603-011-0211-0.

Ye, Z., Ghassemi, A., 2018. Injection-induced shear slip and permeability enhancement in granite fractures. Journal of Geophysical Research: Solid Earth 123, 9009–9032. doi:10.1029/2018JB016045.

Yeo, I., Brown, M., Ge, S., Lee, K., 2020. Causal mechanism of injection-induced earthquakes through the m w 5.5 pohang earthquake case study. Nature communications 11, 1–12. doi:10.1038/s41467-020-16408-0.

Yoon, J.S., Stephansson, O., Zang, A., Min, K.B., Lanaro, F., 2017. Discrete bonded particle modelling of fault activation near a nuclear waste repository site and comparison to static rupture earthquake scaling laws. International Journal of Rock Mechanics and Mining Sciences 98, 1–9. doi:10.1016/j.ijrmms.2017.07.008.

Zang, A., Zimmermann, G., Hofmann, H., Stephansson, O., Min, K.B., Kim, K.Y., 2019. How to reduce fluid-injection-induced seismicity. Rock Mechanics and Rock Engineering 52, 475–493. doi:10.1007/s00603-018-1467-4.

Zhuang, L., Kim, K.Y., Jung, S.G., Diaz, M., Min, K.B., Zang, A., Stephansson, O., Zimmermann, G., Yoon, J.S., Hofmann, H., 2019. Cyclic hydraulic fracturing of pocheon granite cores and its impact on breakdown pressure, acoustic emission amplitudes and injectivity. International Journal of Rock Mechanics and Mining Sciences 122, 104065. doi:10.1016/j.ijrmms.2019.104065.

Zhuang, X., Chun, J., Zhu, H., 2014. A comparative study on unfilled and filled crack propagation for rock-like brittle material. Theoretical and Applied Fracture Mechanics 72, 110–120. doi:10.1016/j.tafmec.2014.04.004.

Zielonka, M.G., Searles, K.H., Ning, J., Buechler, S.R., 2014. Development and validation of fully-coupled hydraulic fracturing simulation capabilities, in: Proceedings of the SIMULIA community conference, SCC2014, pp. 19–21.

Zoback, M., Rummel, F., Jung, R., Raleigh, C., 1977. Laboratory hydraulic fracturing experiments in intact and pre-fractured rock, in: International

Journal of Rock Mechanics and Mining Sciences & Geomechanics Abstracts, Elsevier. pp. 49–58. doi:10.1016/0148-9062(77)90196-6.

Zoback, M.D., 2010. Reservoir geomechanics. Cambridge University Press. doi:10.1017/CBO9780511586477.

Zoback, M.D., Gorelick, S.M., 2012. Earthquake triggering and large-scale geologic storage of carbon dioxide. Proceedings of the National Academy of Sciences 109, 10164–10168. doi:10.1073/pnas.1202473109.

Cacace: Reviewing and Editing, Validation. **Jean Schmittbuhl**: Supervision.

Declaration of interests

☒ The authors declare that they have no known competing financial interests or personal relationships that could have appeared to influence the work reported in this paper.

☐The authors declare the following financial interests/personal relationships which may be considered as potential competing interests:

Modeling of fluid-induced seismicity during injection and after shut-in

Qinglin Deng[1,*], Guido Blöcher[2], Mauro Cacace[2], Jean Schmittbuhl[1]

Highlights

Modeling of fluid-induced seismicity during injection and after shut-in

Qinglin Deng, Guido Blöcher, Mauro Cacace, Jean Schmittbuhl

- A fully hydro-mechanical model is to capture fault slip behavior during injection and after shut-in
- Reproduce fluid induced fault slip after shut-in with no hydraulic connection and with obvious time lag
- Coupled pressure diffusion with poro-elastic stressing can be responsible for the larger magnitude events after shut-in than during injection
- Initial stress state is of central importance for fluid injecion induced seismicity

*Corresponding author
Email address: dengq@unistra.fr (Qinglin Deng)
[1]EOST/ITES, Université de Strasbourg/CNRS, France
[2]GFZ German Research Centre for Geosciences, Potsdam, Germany